Evaluation of six geothermal heat flux maps for the Antarctic Lambert-Amery glacial system

Haoran Kang[1],Liyun Zhao[1,2*], Michael Wolovick[3], John C. Moore[1,4,5*]

[1] College of Global Change and Earth System Science, Beijing Normal University, Beijing 100875, China

[2] State Key Laboratory of Earth Surface Processes and Resource Ecology, Beijing Normal University, Beijing 100875, China

[3] Alfred Wegener Institute, Bremerhaven, Germany

[4] CAS Center for Excellence in Tibetan Plateau Earth Sciences, Beijing 100101, China

[5] Arctic Centre, University of Lapland, Rovaniemi, Finland

* Corresponding author

Corresponding author: Liyun Zhao (zhaoliyun@bnu.edu.cn); John C. Moore (john.moore.bnu@gmail.com)

Abstract

Basal thermal conditions play an important role in ice sheet dynamics, and they are sensitive to geothermal heat flux (GHF). Here we estimate the basal thermal conditions, including basal temperature, basal melt rate, and friction heat underneath the Lambert-Amery glacier system in east Antarctica, using a combination of a forward model and an inversion from a 3D ice flow model. We assess the sensitivity and uncertainty of basal thermal conditions using six different GHF maps. We evaluate the modelled results using all observed subglacial lakes. The different GHF maps lead to large differences in simulated spatial patterns of temperate basal conditions. The two recent GHF fields inverted from aerial geomagnetic observations have the highest GHF, produce the largest warm-based area, and match the observed distribution of subglacial lakes better than the other GHFs. The modelled basal melt rate reaches ten to hundreds of mm per year locally in Lambert, Lepekhin and Kronshtadtskiy glaciers feeding the Amery ice shelf, and ranges from 0-5 mm yr^{-1} on the temperate base of the vast inland region.

1 Introduction

The Lambert-Amery system in East Antarctica is believed to be relatively stable against climate change and has changed little over several decades of observations (King et al., 2007). However, there is also evidence of extensive subglacial canyons and lakes (Fretwell et al., 2013; Jamieson et al., 2016; Cui et al., 2020a). Subglacial canyons and lakes are conduits for subglacial water, transporting subglacial meltwater to the coast through complex hydrologic routing, that may change on relatively fast timescales (Malczyk et al., 2020). Jamieson et al. (2016) report a large subglacial drainage network in Princess Elizabeth Land (PEL), which would transport water from central PEL to the coast passing the Lambert-Amery region. Subglacial water can affect the ice flow

(Stearns et al., 2008; Diez et al., 2018), influence the dynamical stability and basal mass balance (Gudlaugsson et al., 2017), and may enhance basal melt of ice shelves (Le Brocq et al., 2013).

Ice temperature is an important factor in the rheology of ice (Budd et al., 2013) and ice flow. Whether the basal ice is at the melting point influences the movement of the ice to a great extent. Ice at the melting point can lead to water flowing along hydraulic gradients and accumulating in local depressions (Fricker et al., 2016). The meltwater lubricates the ice/bed interface or saturates any sediment till layer, allowing higher ice velocities via basal sliding. For instance, the rapid retreat of Thwaites and Pope glaciers in the Amundsen Sea sector of West Antarctica is being facilitated by high heat flow in the underlying lithosphere (Dziadek et al., 2021). This bed-ice linkage forms the basis for making inferences on basal conditions via surface observations (Pattyn, 2010), or relict landforms (e.g. Näslund et al., 2005).

The ice temperature is controlled by deformational heat generated from strain within the ice, advection of heat due to lateral ice motion and the descent rate of ice from the surface, conduction of heat through the ice and frictional heating from basal sliding. Ice temperature is hard to evaluate because of the scarcity of in-situ measurements, typically obtained from boreholes that are very rarely drilled through the Antarctic ice sheet. GHF is an important boundary condition for ice temperature simulation, and is generally the largest source of uncertainty. Hence geophysical survey methods are used to indirectly map GHF. To date GHF datasets have been estimated from seismic models (Shapiro and Ritzwoller, 2004; An et al., 2015; Shen et al., 2020), derived from airborne magnetic surveys (Li et al., 2021; Martos et al., 2017) and satellite geomagnetic data (Maule et al., 2005; Purucker, 2013).

Extensive ice penetrating radar data has been collected recently over Princess Elizabeth Land (PEL; Fig. 1d), including the eastern part of the Lambert-Amery system (Cui et al., 2020a). This fills in large data gaps from older surveys, and provides the basis for our study. The radar surveys reveal ~1100 km long canyons (Fig. 1c) that are incised hundreds of meters deep into the subglacial bed that extend from the Gamburtsev Subglacial Mountains (GSM) to the coast of the Western Ice Shelf (WIS). Li et al. (2021) collected airborne magnetic data that can be combined with radar ice thicknesses and estimated depths at which the bedrock reaches its Curie temperature, to invert for the geothermal flux. The resulting higher resolution data set (Li et al., 2021) implies a larger heat flux than previous estimates in this region. Furthermore, recently discovered subglacial lakes, including potentially the second largest subglacial lake in Antarctica, add evidence for more widespread basal melting in the region than was thought based on the much sparser earlier survey data (Cui et al., 2020b). The complex subglacial topography, relatively high geothermal heat flux and subglacial lakes imply a complex distribution of basal thermal conditions and subglacial water networks. These heterogenous basal conditions will have shaped much of the ice flow and mass balance of the Lambert-Amery system. This motivates us to investigate how the basal thermal

conditions inferred from the new high-resolution topography dataset (Cui et al., 2020a) can be reconciled with surface ice velocities and existing geothermal heat flow maps.

Ice sheet models can be used to simulate the dynamics and thermodynamics of the ice sheet. Glaciologists have combined ice sheet models with measurements of vertical temperature profiles or thawed basal states to constrain GHF of the ice sheets (e.g. Pattyn, 2010; Rezvanbehbahani et al., 2019). In the Lambert-Amery glacial system, Pittard et al. (2016) suggest that ice flow is most sensitive to the spatial variation in the underlying GHF near the ice divides and along the edges of the ice streams.

In this study, we simulate ice basal temperatures and basal melt rates in the Lambert-Amery system using the new high-resolution digital elevation model, along with six different published GHF maps as forcing for an off-line coupling between a basal energy and water flow model and a 3D full-Stokes ice flow model. We evaluate the quality of the resulting basal temperature field incorporating the Stokes model estimates of ice advection, strain and frictional heating under the different GHF maps using all available observed subglacial lakes and surface velocities. Hence, we make inferences on which GHF maps yield the best match with observations in the region.

2 Regional Domain and Datasets

Our modeled domain is part of the Lambert-Amery system. It consists of two drainage basins: the Lambert Glacier Basin, the American Highland Basin, along with about half of the Amery Ice Shelf (Fig. 1). The 2D domain boundary outlines are defined by the inland ice catchment basin boundary, the central streamline, and the ice front of Amery Ice Shelf. The central streamline was chosen by selecting a point at the confluence of Lambert Glacier and Lepekhin Glaicer and then advecting that point downstream to the ice front using the observed velocity field. The margins of the inland sub-basin and the central streamline of the Amery Ice Shelf were chosen as boundaries because the mass flux across them is assumed to be zero by definition.
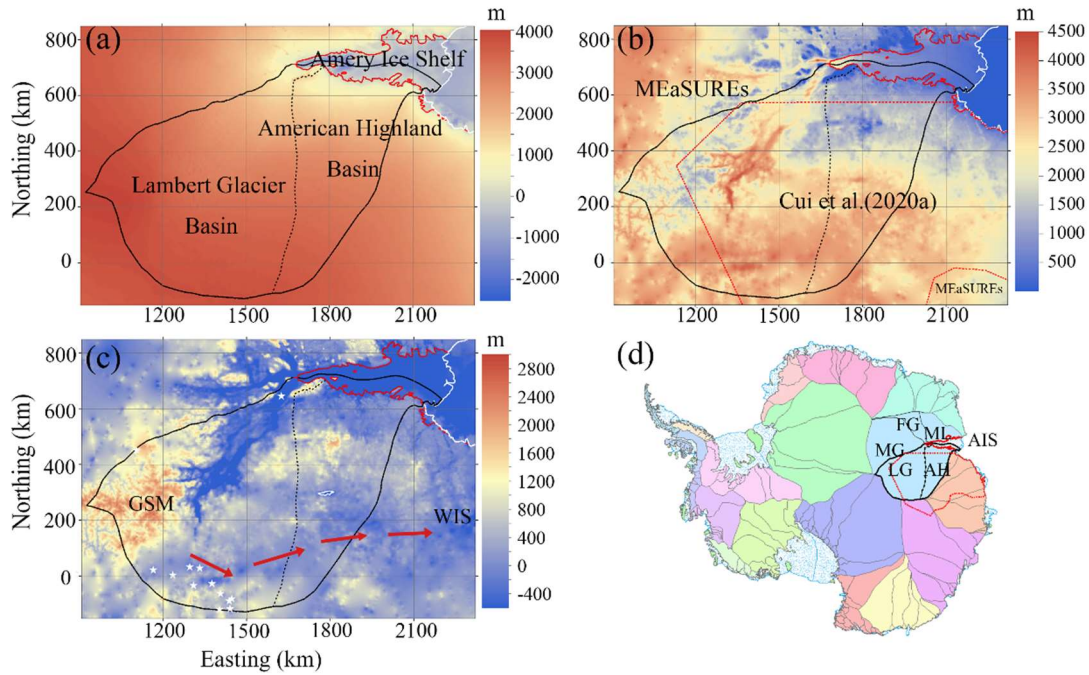
Fig. 1. The domain topography and location with domain boundary overlain. (a) surface elevation; (b) ice thickness; (c) bed elevation; (d) the location of our domain in Antarctica. The solid black curve is the outline of the study domain, including the central streamline of Amery ice shelf and the boundary of inland sub-basins based on drainage-basin boundaries defined from satellite ice sheet surface elevation and velocities (Mouginot et al., 2017; Rignot et al., 2019). The solid red and white curves in (a-c) are the grounding line and margin of Antarctic respectively (Morlighem et al., 2020). The dotted black curve is the dividing line between Lambert Glacier Basin and the American Highland Basin. The dotted red curves in (b) and (d) are the boundary of ice thickness data from Cui et al. (2020a), inside which we incorporates data from Cui et al. (2020a), and outside from MEaSUREs BedMachine Antarctica, version 2. The white stars in (c) denote the locations of observed subglacial lakes (Wright and Siegert, 2012; Cui et al., 2021), and the region within the white line at (1800E, 300N) is potentially the second largest subglacial lake in Antarctic. The red arrows in (c) indicate the routing through the deep subglacial canyon system from GSM to WIS. The sub-basins names of Lambert-Amery system are labeled in (d), ML for MacRobertson Land basin, FG for Fisher glacier basin, MG for Mellor glacier basin, LG for Lambert glacier basin, AH for American Highland basin, and AIS for Amery Ice Shelf.

The surface elevation, bedrock elevation, and ice thickness from Cui et al. (2020a) are used in most of the domain (Fig. 1b; Table 1) with additional data are from MEaSUREs BedMachine Antarctica, version 2 at a resolution of 500 m (Morlighem et al., 2020). The bed elevation is calculated by subtraction of the ice thickness from the surface elevation.

The surface ice velocity data are obtained from MEaSUREs InSAR-based Antarctic ice velocity Map, version 2 with resolution of 450 m (Rignot et al., 2017). Data were largely acquired during the International Polar Years 2007 to 2009, and between 2013 and 2016. Additional data acquired between 1996 and 2016 were used as needed to maximize

144   coverage.
145
146   Ice sheet surface temperature data are prescribed by ALBMAP v1 with a resolution of
147   5 km (Le Brocq et al., 2010) and come from monthly estimates inferred from AVHRR
148   data averaged over 1982-2004. Subglacial lake locations are from the fourth inventory
149   of Antarctic subglacial lakes (Wright and Siegert, 2012), with the addition of the newly
150   discovered lakes (Cui et al., 2020b).
151
152   Six GHF datasets (Fig. 2; Table 2) are used in this study. All the datasets are interpolated
153   into the same 2.5 km resolution.
154
155   Table 1 Datasets used in this study.

Variable name	Dataset	Resolution	Reference
surface elevation, bedrock elevation, and ice thickness	MEaSUREs BedMachine Antarctica version 2	500 m	Morlighem et al., 2020; Cui et al., 2020
surface ice velocity	MEaSUREs InSAR-based Antarctic ice velocity Map, version 2	450 m	Rignot et al., 2017
surface temperature	ALBMAP v1	5 km	Le Brocq et al., 2010;
subglacial lakes location	The fourth inventory of Antarctic subglacial lakes	-----	Wright and Siegert, 2012; Cui et al., 2021

156

157   Table 2 The six GHF datasets used in this study.

GHF map	Reference	Method	Mean (mW m^{-2})	Range (mW m^{-2})
Martos	Martos et al., 2017	airborne geomagnetic data	72	47-90
Shen	Shen et al., 2020	seismic model	50	43-59
An	An et al., 2015	seismic model	55	40-66
Shapiro	Shapiro and Ritzwoller, 2004	seismic model	54	45-58
Purucker	Purucker, 2013	Satellite geomagnetic data	47	26-47
Li	Li et al., 2021	airborne geomagnetic data	72	52-90

158
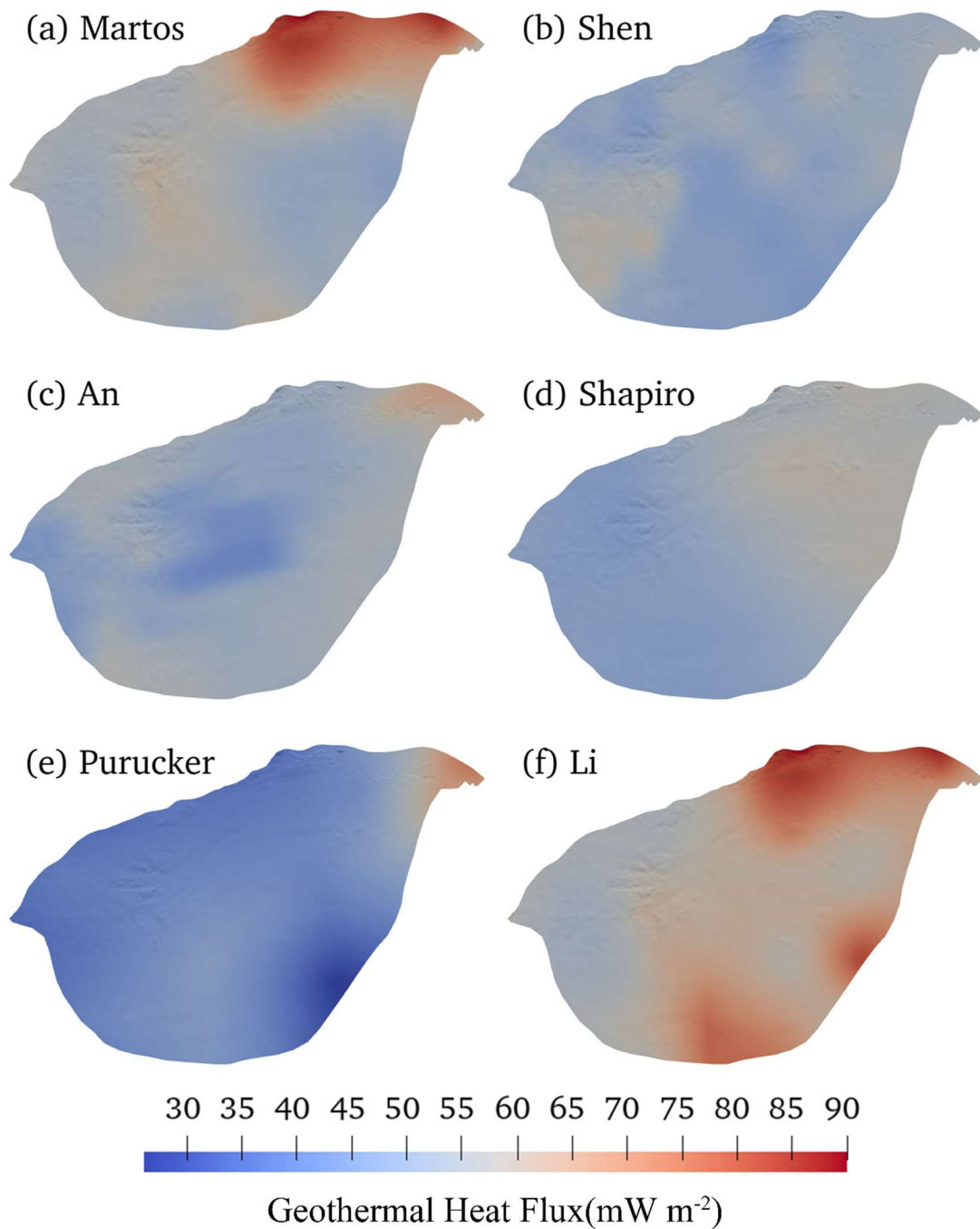
Fig. 2. The spatial distribution of GHF over our domain as described in Fig. 1. See Table 2 for the GHF map details.

3 Model

Our goal is to infer the basal thermal conditions, including basal temperature and basal melt rate in the domain. Geothermal heat flux, englacial heat conduction and basal friction heat are the main heat sources that determine the basal thermal conditions. Therefore, we need to model both ice flow velocity and stress for basal friction heat and

168 ice temperature for englacial heat conduction.

169

170 We solve an inverse problem by a full-Stokes model, implemented in Elmer/Ice, to infer
171 the basal friction coefficient such that the modelled velocity best fits observations
172 (Gagliardini et al., 2013). Using the best-fit basal friction coefficient, we obtain the ice
173 flow velocity, stress and basal friction heat. A proper initial vertical ice temperature
174 profile subject to thermal boundary conditions is needed in solving the inverse problem.
175 To get it, we use a forward model that consists of an improved Shallow Ice
176 Approximation (SIA) thermomechanical model with a subglacial hydrology model
177 (Wolovick et al., 2021a). The forward model uses the modelled velocity direction and
178 basal slip ratio from the full-Stokes inverse model to constrain its solution. We do steady
179 state simulations by coupling the forward and inverse models. We will describe the
180 forward model in Section 3.1 and the inverse model in Section 3.2, then the coupling
181 in Section 3.3.

182 **3.1 Forward Model**

183 The forward model consists of a thermomechanical steady state model using an
184 improved Shallow Ice Approximation (SIA) in equilibrium with the subglacial
185 hydrological system (Wolovick et al., 2021a). It has internal consistency between three
186 components: ice flow, ice temperature, and basal water flux. The numerical model
187 requires three coupled components to be consistent with one another: (1) integration for
188 balance flux and englacial temperature downhill along the ice surface, (2) integration
189 for basal water flux and freezing rate downhill in the hydraulic potential, and (3)
190 rheology and shape function computations to determine the distribution of ice flux and
191 shear heating. The model performs a fixed-point iteration for consistency between
192 these three components. In addition. we improve on the model used in Wolovick et al.
193 (2021a) by combining the observed velocity field, the velocity field from the full-Stokes
194 model, and the surface gradient direction to compute a merged surface flow direction
195 field. The observations are used where flow is fast, Elmer/Ice modelled velocity is used
196 where flow is slow, and the surface gradient is only used near the margins of the domain
197 where the Elmer velocity field is not reliable (Fig. 3). The simulation is done on a finite
198 difference mesh with resolution of 2.5 km.

199

200 The surface accumulation rate we used in the forward thermal model is the mean of
201 Arthern et al. (2006) and Van de Berg et al. (2005). Both were accessed through the
202 ALBMAP_v1 dataset (Le Brocq et al., 2010).

203

204 One key complexity is how to deal with basal thermal boundary condition. At the
205 bottom of ice shelves, we set basal temperature equal to the pressure melting point. At
206 the bed of grounded ice, the boundary condition can be either Dirichlet or Neumann
207 condition depending on the basal melting and subglacial water conditions. The basal
208 boundary conditions are given by,

$$-k(T)\frac{dT}{dz} = G, \quad \text{for } T < T_m \text{ and } m = 0; \tag{1}$$

$$\text{T} = T_m, \quad \text{for } m \neq 0, \tag{2}$$

where $k(T)$ is the temperature-dependent thermal conductivity of ice, m is the basal melt rate, T_m is the pressure-dependent melting temperature, G is GHF, taking six GHF datasets listed in Table 2. The thermal condition will switch from Neumann (Eq 1) to Dirichlet (Eq 2) if the basal temperature exceeds the pressure-dependent melting point. The opposite switch from Dirichlet to Neumann is determined by the hydrology model, if there is insufficient water input to supply a large freezing rate.
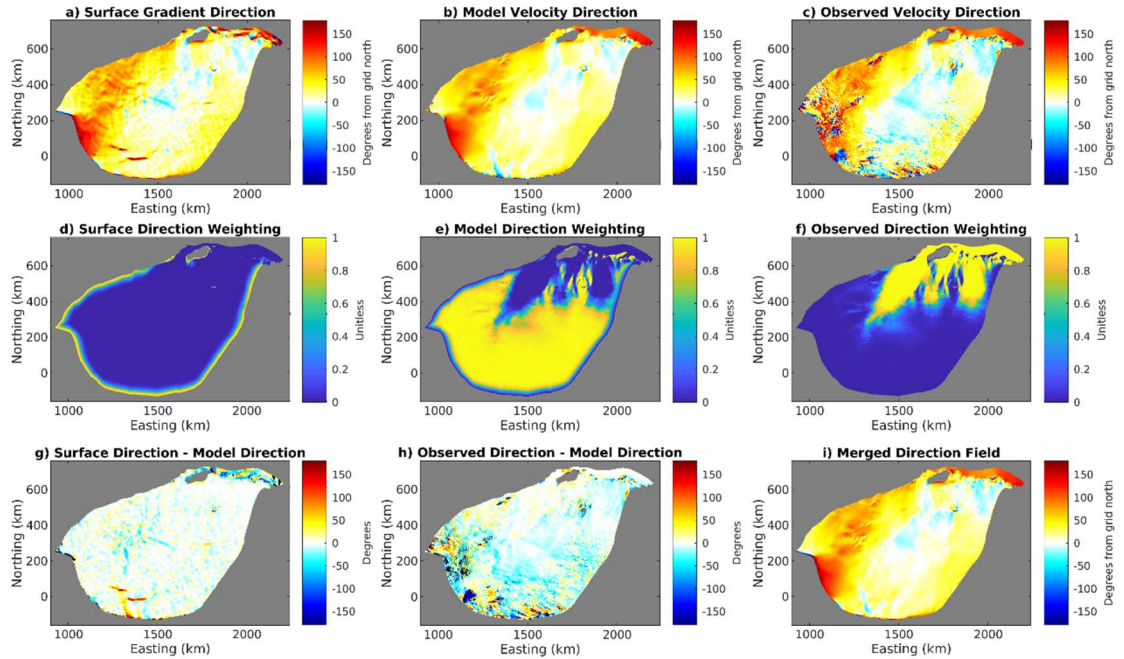
Fig. 3. Surface velocity direction fields, in degrees clockwise from grid north. The first row shows the direction from surface gradient (a), Elmer/Ice modelled velocity (b), and the observed velocity direction (c). The middle row (d-f) shows the 3 corresponding weighting fields (the sum of these weights is 1). The bottom row shows the difference between the direction of surface gradient and Elmer/Ice modelled velocity (g), the difference between the observed velocity direction and Elmer/Ice modelled velocity h), and the merged velocity field used in the forward model (i).

One improvement on the method from Wolovick et al. (2021a) is that a temperate basal ice layer with non-zero thickness is permitted in our model in the case that the modelled basal ice temperature reaches the pressure melting point. We do this using a weak-form solution in which the volumetric englacial melt rate rises steeply as temperature exceeds the melting point. The englacial melting absorbs latent heat and serves to limit temperature rise. We parameterize the increase in volumetric melt rate as an exponential function of temperature with a 1 K e-folding temperature, and a prefactor given by the englacial strain heating and the latent heat of fusion. All englacial meltwater generated this way is assumed to immediately drain to the bed.

Another key component of the forward model is the shape function determining the

distribution of horizontal velocity with depth. We also improve the shape function in Wolovick et al. (2021a) by including the basal slip ratio, $\hat{u}_b = u_b / \bar{u}$, where u_b is the basal velocity magnitude and $\bar{u}$ is the vertically averaged horizontal velocity magnitude. The slip ratio is taken from the full-Stokes inverse model. Other than the addition of a spatially variable slip ratio, the shape function calculation is unchanged from Wolovick et al. (2021a).

3.2 Inverse Model with full-Stokes Model

The spatial distribution of basal friction in the domain is modelled by solving an inverse problem using the three-dimensional the full-Stokes model, Elmer/Ice, an open source finite element method package (Gagliardini et al., 2013). The inverse model is based on adjusting the spatial distribution of the basal friction coefficient to minimize the misfit between simulated and observed surface velocities. The modelled velocity is obtained by solving the full-Stokes equation, which includes conservation equations for both the momentum and mass of the ice,

$$\nabla \cdot \boldsymbol{\tau} - \nabla p = \rho_i \vec{g}, \tag{3}$$

$$\nabla \cdot \vec{v} = 0, \tag{4}$$

where $\boldsymbol{\tau}$ is the deviatoric stress tensor, p is the isotropic pressure, ρ_i is ice density, $\vec{g}$ is the acceleration due to gravity (0, 0, -9.81) m s^{-2}, $\vec{v}$ is ice velocity. According to Glen's flow relation, deviatoric stress is related to the deviatoric part of the strain rate tensor, $\dot{\varepsilon}_E$, which can be described by $\boldsymbol{\tau} = 2\eta\dot{\varepsilon}_E$, where the effective viscosity of the ice, η, is sensitive to the temperature-dependent flow rate factor *A(T)* calculated using an Arrhenius equation (Cuffey and Paterson, 2010). The ice temperature distribution comes from the forward model in section 3.1.

3.2.1 Mesh Generation and Refinement
Firstly, we use GMSH (Geuzaine and Remacle, 2009) to generate an initial 2-D horizontal footprint mesh with the boundary described in section 2. Then we refine the mesh by an anisotropic mesh adaptation code called the Mmg library (http://www.mmgtools.org/). The resulting mesh is shown in Fig. 4 and has minimum and maximum element sizes of approximately 1000 m and 8000 m. The 2-D mesh is then vertically extruded using 10 equally spaced, terrain following layers.
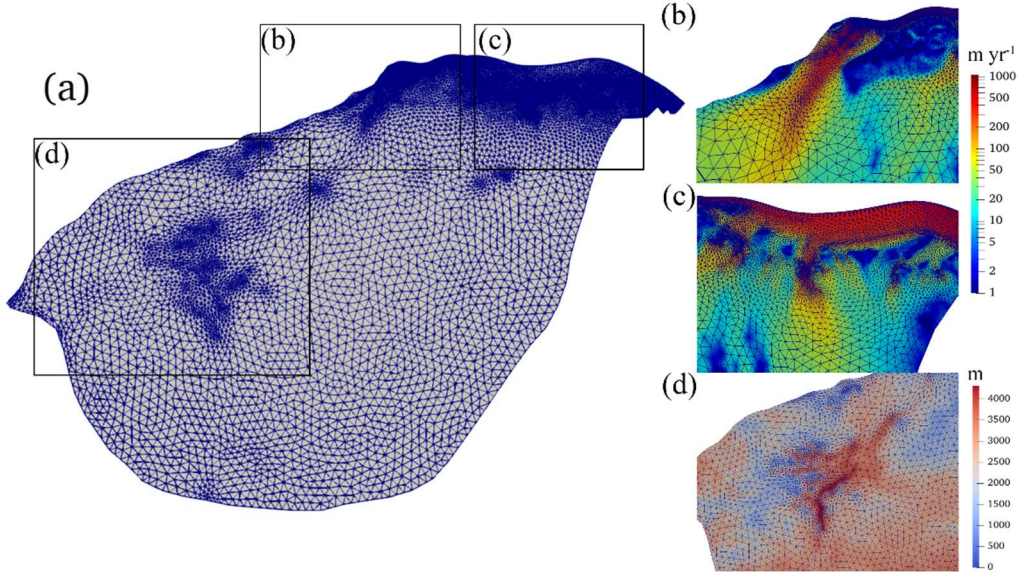
268 Fig. 4. The refined 2-D horizontal domain footprint mesh (a). Boxes outlined in (a) are shown in
269 detail overlain with surface ice velocity in (b) and (c), and with ice thickness in (d).
270

3.2.2 Boundary Condition

272 The ice surface is assumed to be stress-free. At the ice front, the normal stress under the
273 sea surface is equal to the hydrostatic water pressure. On the lateral boundary, the
274 normal stress is equal to the ice pressure applied by neighboring glaciers and the normal
275 velocity is assumed to be 0. The bed for grounded ice is assumed to be rigid,
276 impenetrable, and fixed over time. Since we perform a stress-balance snapshot in the
277 full-Stokes model, we do not need to prescribe surface mass balance or basal mass
278 balance in the boundary conditions.
279

280 The normal basal velocity is set to 0 at the ice-bed interface. The linear sliding law is
281 used to describes the relationship between the basal sliding velocity, $\vec{u}_b$, and the basal
282 shear force, $\vec{\tau}_b$, on the bottom of grounded ice,

$$\vec{\tau}_b = C \ \vec{u}_b. \tag{5}$$

284 To avoid non-physical negative values, $C = 10^{\beta}$ is used in the simulation. We call β
285 the basal friction coefficient rather than C. C is initialized to a constant value of 10^{-4}
286 MPa m^{-1} yr (Gillet-Chaulet et al., 2012), and then replaced with the inverted C in
287 subsequent inversion steps.
288

3.2.3 Surface Relaxation

290 We relax the free surface of the domain by a short transient run to reduce the non-
291 physical spikes in initial surface geometry (Zhao et al., 2018). The transient simulation
292 period here is 0.5 yr with a timestep of 0.01 yr.
293

3.2.4 Inversion and Improvement for Basal Friction Coefficient

295 Taking the results from the surface relaxation as our ice geometry we use an inverse

model to retrieve the basal friction coefficient, the deviatoric stress field and ice velocity field. The inverse model adjusts the spatial distribution of the basal friction coefficient to minimize the value of the cost function (Morlighem et al., 2010), which is defined as the difference between the simulated surface velocity and the observed,

$$J_0 = \int_{\Gamma_s} \frac{1}{2}\left(|\vec{u}| - |\vec{u}_{obs}|\right)^2 d\Gamma \tag{6}$$

where Γ_s is the ice surface, $\vec{u}$ and $\vec{u}_{obs}$ are the simulated and observed surface velocities.

To avoid over-fitting of the inversion solution to non-physical noise in the observations, a regularization term,

$$J_{reg} = \frac{1}{2}\int_{\Gamma_s}\left(\left(\frac{\partial C}{\partial x}\right)^2 + \left(\frac{\partial C}{\partial y}\right)^2\right)d\Gamma, \tag{7}$$

is added to the cost function, then the total cost function is defined as,

$$J_{tot} = J_0 + \lambda J_{reg}, \tag{8}$$

where λ is a positive regularization weighting parameter. An L-curve analysis (Hansen and Johnston, 2000) has been carried out for inversions to find the optimal λ by plotting the term J_{reg} as the function of J_0. The optimal value of 10^{10} is chosen for λ to minimize J_0.

Basal friction in reality depends on basal temperature, i.e., it is relatively large on cold beds since the ice is frozen, and small on warm bed where basal temperature reaches pressure-melting point allowing the ice to slide (Greve and Blatter, 2009). However, in the inverse model, basal friction coefficient (Eq 5) is adjusted to match velocity observations without regard to basal temperature, which leads to unrealistic noise manifested as local spikes in modelled basal friction heat (Fig. 5a).

We improve the parameterization of β via C in Eq 5 (Section 3.2.2) by considering basal temperature T_{bed},

$$\beta_{new} = \beta_{old} + \alpha(T_m - T_{bed}), \tag{9}$$

where β_{old} is from the inverse model, α is a positive factor to be tuned, T_m is pressure-dependent melting temperature. β_{new} equals β_{old} at a bed with temperate ice, and is larger than β_{old} at a bed with ice temperature lower than T_m. We tune α in the range of [0.1, 2] with an interval of 0.1, and find the local spikes in modelled friction heat become fewer (Fig. 5) as α increases from 0.1 to 1, but stay almost constant with α from 1 to 2. Therefore, we take α to be 1, and use the parameterization of β_{new} in Eq 5 in all the simulations. Using Eq 9, the difference of simulated and observed surface velocity is unchanged over the region except for some parts of the inland boundary.
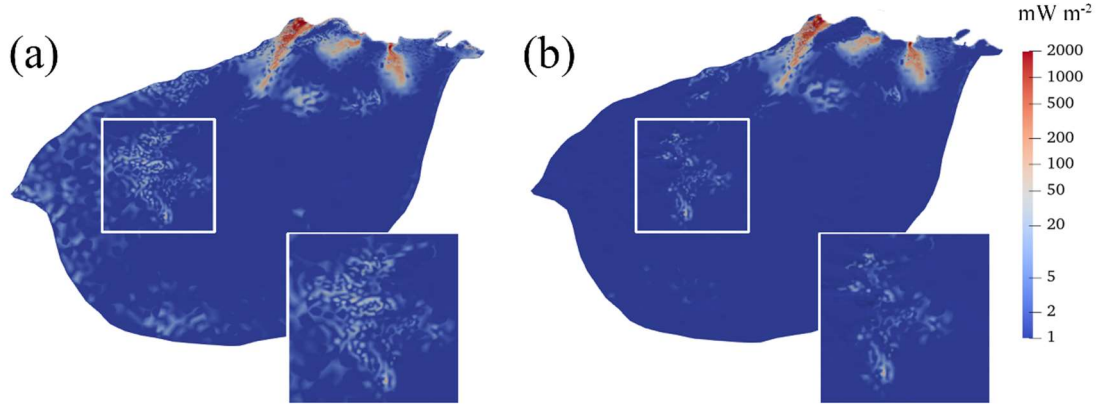
332 Fig. 5. Comparison of modelled basal friction heat with basal friction coefficient β_{old} (a) and β_{new}
333 with α=1 (b) driven by Martos et al. (2017) GHF. The white square is enlarged.

3.2.5 Basal Melt Rate

Based on the inverted basal velocity and basal shear stress, we can calculate the basal friction heat. We then produce the basal melt rate using the thermal equilibrium as follows (Greve and Blatter, 2009):

$$M = \frac{G + \vec{u}_b \vec{\tau}_b + k(T)\frac{dT}{dz}}{\rho_i L}, \tag{10}$$

where M is the basal melt rate, G is GHF, $\vec{u}_b \vec{\tau}_b$ is the basal friction heat, $-k(T)\frac{dT}{dz}$ is

the upward heat conduction, ρ_i is the ice density, and L is latent heat of ice melt.

Geothermal heat and frictional heating from basal slip warm the base, while the upward heat conduction to the interior cools the base. Note that basal melt rate can be either positive (melting) or negative (freezing) depending on the heat balance.

3.3 Experimental Design of coupled simulations

We design the coupled simulations in an 8-step scheme for coupling the forward model and inverse model similar to Zhao et al. (2018):
1. We run the forward model with the velocity direction taken from a mixture of the surface gradient and surface velocity observations, and get an initial modelled englacial temperature (Fig. 3).
2. We do surface relaxation in Elmer/Ice with the englacial temperature from step 1.
3. Taking the results from step 2 as the initial state, we do an inversion in Elmer/Ice using the modeled englacial temperature from step 1, to get a modelled surface velocity best fit to the observed surface velocity. The modelled surface velocity will remove some artifacts in the observed field.
4. We run the forward model using the velocity directions derived by merging the

Elmer/Ice modelled velocity, the surface gradient and the surface velocity observations (Fig. 3). We use the modelled velocity from the full-Stokes inverse model to constrain the basal slip ratio, then constrain rheology and shape function in the forward model. Then we get an updated modelled englacial temperature.

5. We run the inverse model in Elmer/Ice with the improved englacial temperature from step 4, and get an updated modelled velocity.

6. We run the forward model again using the ratio of basal sliding to column-average velocity in Elmer/Ice from step 5 to constrain the slip ratio, and get a further updated basal temperature.

7. We run the inverse model again in Elmer/Ice with the improved englacial temperature from step 6, and get an updated modelled velocity and stress.

8. We analyze the modelled results in step 7, calculate basal friction heat and basal melt rate.

We perform the above procedure for all six sets of GHF to produce six different results for the basal thermal conditions.

4 Simulation Results

4.1 Ice Velocity

In the inverse model, the misfit between the modeled and the observed surface velocity is minimized. Therefore, we get very similar distributions of modeled surface velocity field using different GHF maps. Fig. 6 shows the modelled velocity in the experiment using Martos et al. (2017) GHF as an example. The modeled surface velocity shows spatial similarities to the observed surface velocity (Fig. 6a, b). Three fast-flowing outlet glaciers (Lambert Glacier, Lepekhin Glacier and Kronshtadtskiy Glacier) deliver ice to the ice shelf. The velocity of the Lambert glacier exceeds 800 m yr^{-1} at the grounding line. The Lepekhin Glacier and the Kronshtadtskiy Glacier have maximum flow velocities of about 200 and 400 m yr^{-1} at their grounding lines, respectively. Regions with large differences between modeled and observed surface velocity occupy a small fraction of the whole area (Fig. 6c) and are associated with high velocity gradients. Ice velocity decreases with depth. Fig. 6c shows modeled basal ice velocity. The maximum basal velocity on Lambert Glacier exceeds 500 m yr^{-1} near the grounding line, and maximum basal velocities on Lepekhin Glacier and the Kronshtadtskiy Glacier reach about 150 and 200 m yr^{-1} at the grounding line.
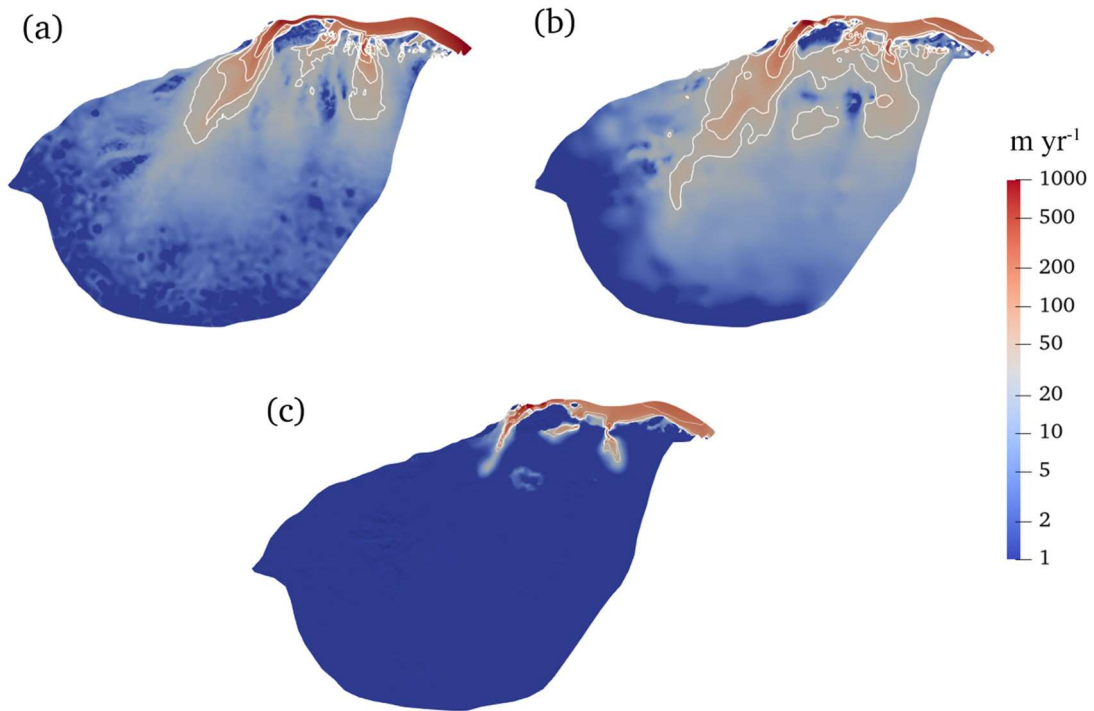
Fig. 6. (a) Observed surface velocity, (b) modeled surface velocity in the experiment using Martos et al. (2017) GHF, (c) modeled basal velocity. The white solid lines in (a), (b), and (c) represent speed contours of 30, 50, 100 and 200 m yr^{-1}, respectively. The three fast-flowing outlet glaciers in plot (a) from left to right are Lambert, Lepekhin and Kronshtadtskiy glaciers.

4.2 Basal Ice Temperature and Heat Conduction

In Fig. 7 we show the modelled basal temperature from the six experiments. The modelled ice basal temperatures in the fast-flowing regions are all at the pressure melting point ("warm"). However, there are significant differences in the modelled distribution of warm-based conditions in the slow-flowing region using different GHF maps. The basal temperature is highly dependent on the GHF. In the experiment using Li et al. (2021) GHF (Fig. 7f), which has the highest GHF within the domain, the basal temperature is at the melting point over most of the domain, with extensive cold based regions confined to the southern part. The experiment using Martos et al. (2017) GHF (Fig. 7a), which has the second highest GHF, yields the second largest area of warm base, and the experiment using Purucker (2013) GHF (Fig. 7e), with the lowest GHF gives the smallest warm-based area which is concentrated around the fast-flowing ice. All experiments display cold basal temperatures to the southwest of the Lambert Glacier Basin, associated with thin ice over subglacial mountains (Fig. 1c).
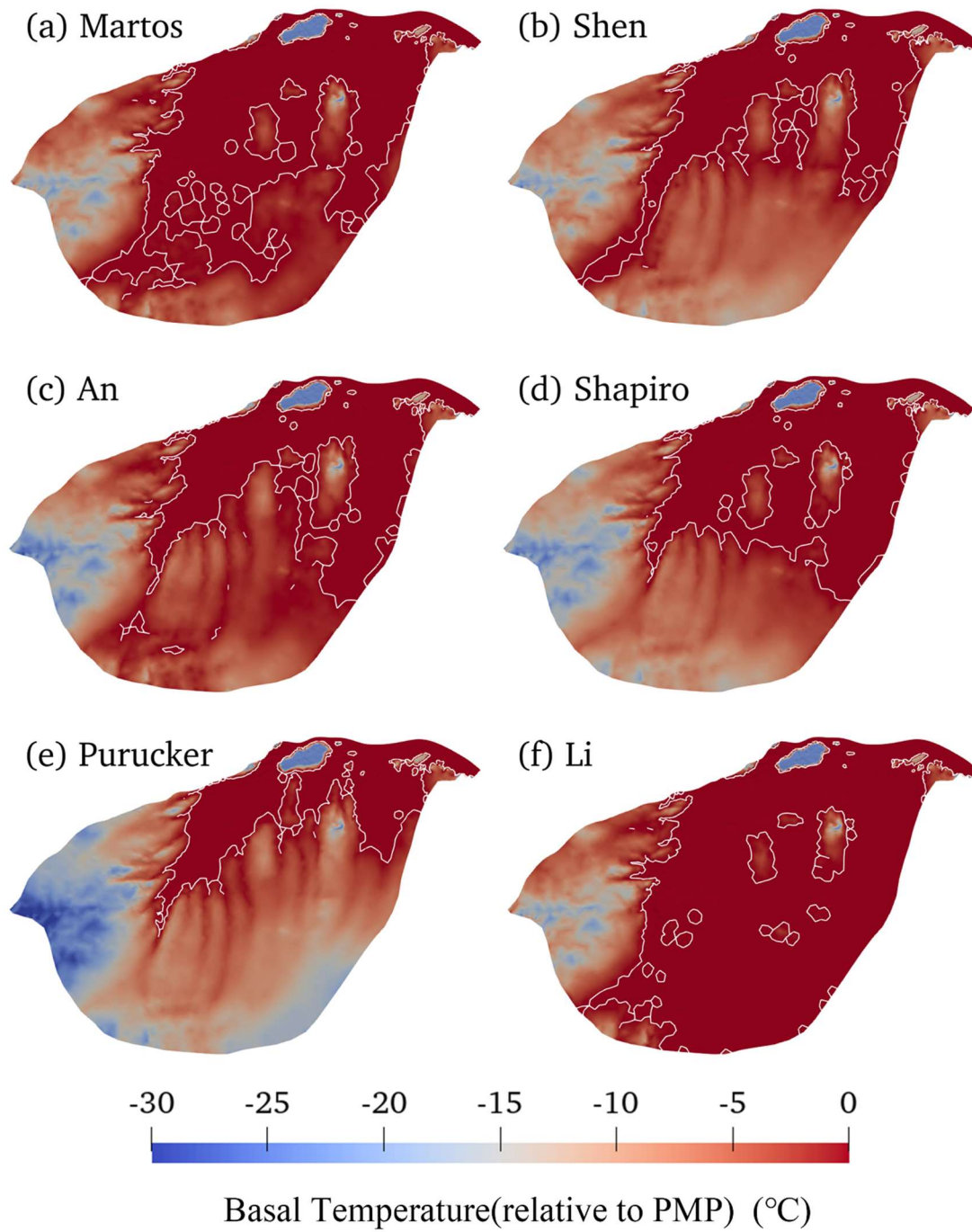
411
Fig. 7. Modelled basal temperature relative to pressure melting point, (a) to (f) corresponding to the
GHF (a) to (f) in Fig. 2. The ice bottom at the pressure-melting point is delineated by a white contour.
414
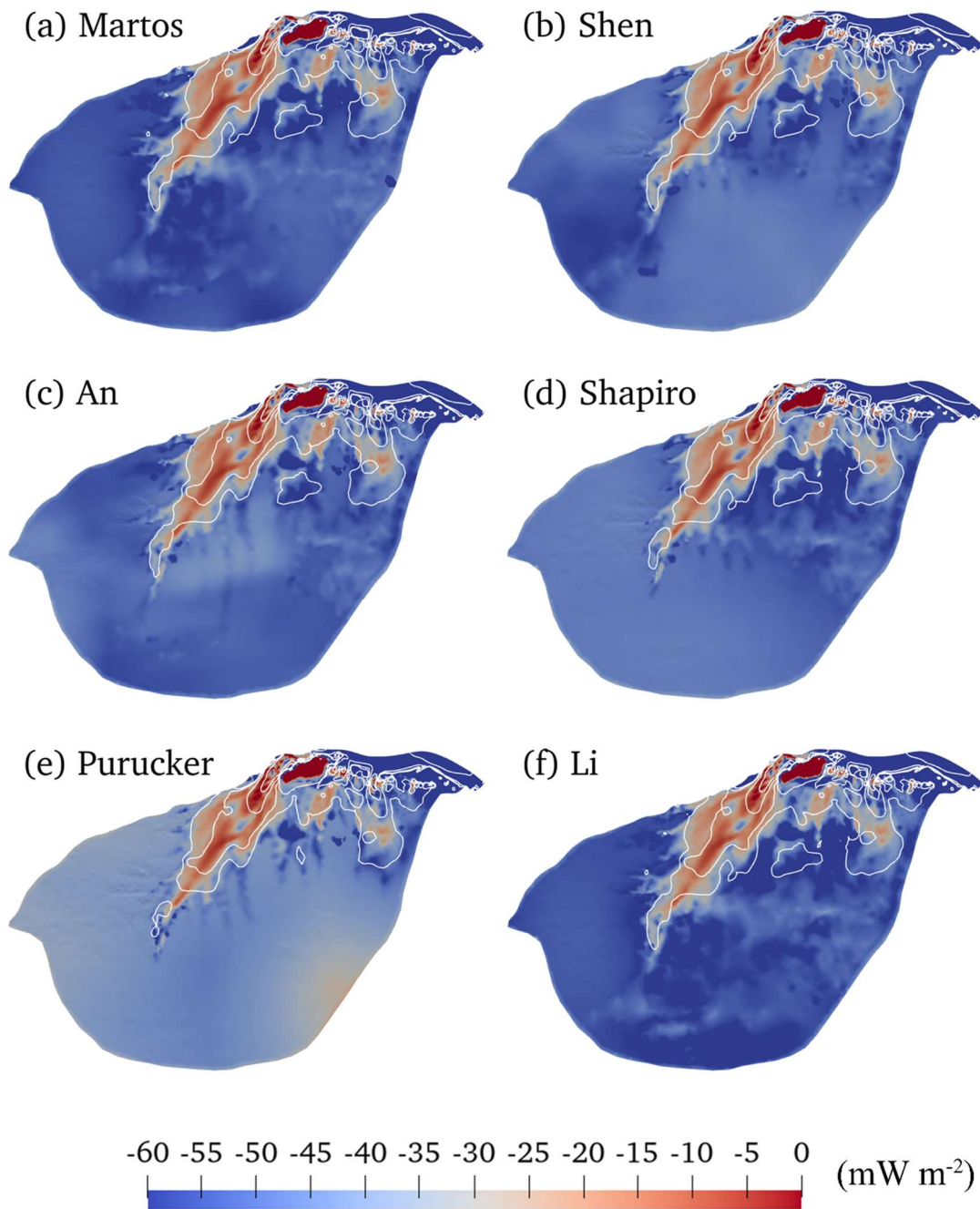
Fig. 8. Modelled heat change of basal ice by upward englacial heat conduction (unit: mW m^{-2}). The negative sign means that the upward englacial heat conduction causes heat loss from the basal ice as defined by the color bar with cooler colors representing more intense heat loss by conduction. (a) to (f) corresponding to the GHF (a) to (f) in Fig. 2. The white solid curves represent modelled speed contours of 30, 50, 100 and 200 m yr^{-1}, the same as in Fig. 6b.

Fig. 8 show the modelled heat change of basal ice by upward englacial heat conduction in the six experiments. In most regions of the fast-flowing tributaries with velocity higher than 30 m yr^{-1}, the heat loss caused by upward basal heat conduction is lower than 30 mW m^{-2} in all experiments, reflecting the development of a temperate basal

layer that limits the basal thermal gradient. For the vast inland areas, experiments yield heat loss by upward heat conduction in the range of 45-60 mW m^{-2} except for the experiment driven by the Purucker (2013) GHF which has lower values around 30-45 mW m^{-2}. This is because the upward heat conduction equals GHF where basal temperature is below the pressure melting point, and the Purucker (2013) GHF is lower than the others.

4.3 Basal Friction Heat

There is no significant difference in modelled basal friction heat across these 6 experiments, reflecting the fact that all of them have been tuned to match the surface velocity observations. So, we show only the modelled basal friction driven by Martos et al. (2017) GHF (Fig. 5b). As expected, basal friction heat is high in fast-flowing regions. The three fast-flowing tributaries have friction heat amounting to more than 50 mW m^{-2}, with the Lambert and Kronshtadtskiy glaciers having 2000 mW m^{-2} at the grounding line.

4.4 Basal Melt Rate

We get the basal melt rate using the thermal balance equation (Eq 10). Fig. 9 shows the modelled basal melt rate in the six experiments using different GHF maps. Regions with basal melt rate coincide with a warm base where basal temperatures reach the pressure-melting point. There are significant differences in the area of basal melting among the six experiments due to large variability in GHF. The experiments using Li et al. (2021) and Martos et al. (2017) GHF yield the largest area with basal melting. In contrast, the experiment using Purucker (2013) GHF gives the least area with basal melting (Fig. 9).

The modelled basal melt rate is below 5 mm yr^{-1} in the parts of the vast inland region that are warm based. Higher basal melt rates occur in fast-flowing regions (Fig. 9) where frictional heat is high (Fig. 5b), despite the differences in GHF (Fig. 2). Basal melt rate is above 10 mm yr^{-1} near the grounding line, reaching 500 mm yr^{-1} at the grounding line of the central flowline running onto Amery ice shelf. Thus, in fast-flowing regions, frictional heat is the dominant factor rather than GHF, consistent with Larour et al. (2012) who noted that slower flowing ice in the interior of the ice sheet will be more sensitive to the GHF, but frictional heat dominates GHF in regions of fast ice flow.

We use the positions of observed subglacial lakes to validate simulated regions with basal melting (Fig. 9). The modelled warm base in the experiment using Li et al. (2021) GHF covers all the observed subglacial lakes in the domain (Fig. 9f), including the recently discovered second-largest subglacial lake in Antarctica (Cui et al., 2020b). The warm base in the experiment using Martos et al. (2017) GHF covers the second greatest number of observed subglacial lakes (Fig. 9a), and the experiment using An et al. (2015) GHF the third (Fig. 9c). The experiment using Shen et al. (2020) GHF captures two subglacial lakes in the southwest of the domain (Fig. 9b), while the experiment using

Shapiro and Ritzwoller (2004) GHF missed many known subglacial lakes in the southwest of the domain, but successfully captures the recently discovered second-largest subglacial lake (Fig. 9b, d). The experiment using Purucker et al. (2013) GHF performs worst in recovering subglacial lake locations (Fig. 9e).

There are localized negative values of basal melt rate, indicating basal refreezing at three locations (Fig. 9). The modelled refreezing locations are generally characterized by large gradients in ice thickness, typically thinning by 700 m across a distance of 2 km. Radar surveys have not yet been carried out to confirm these freeze-on locations.
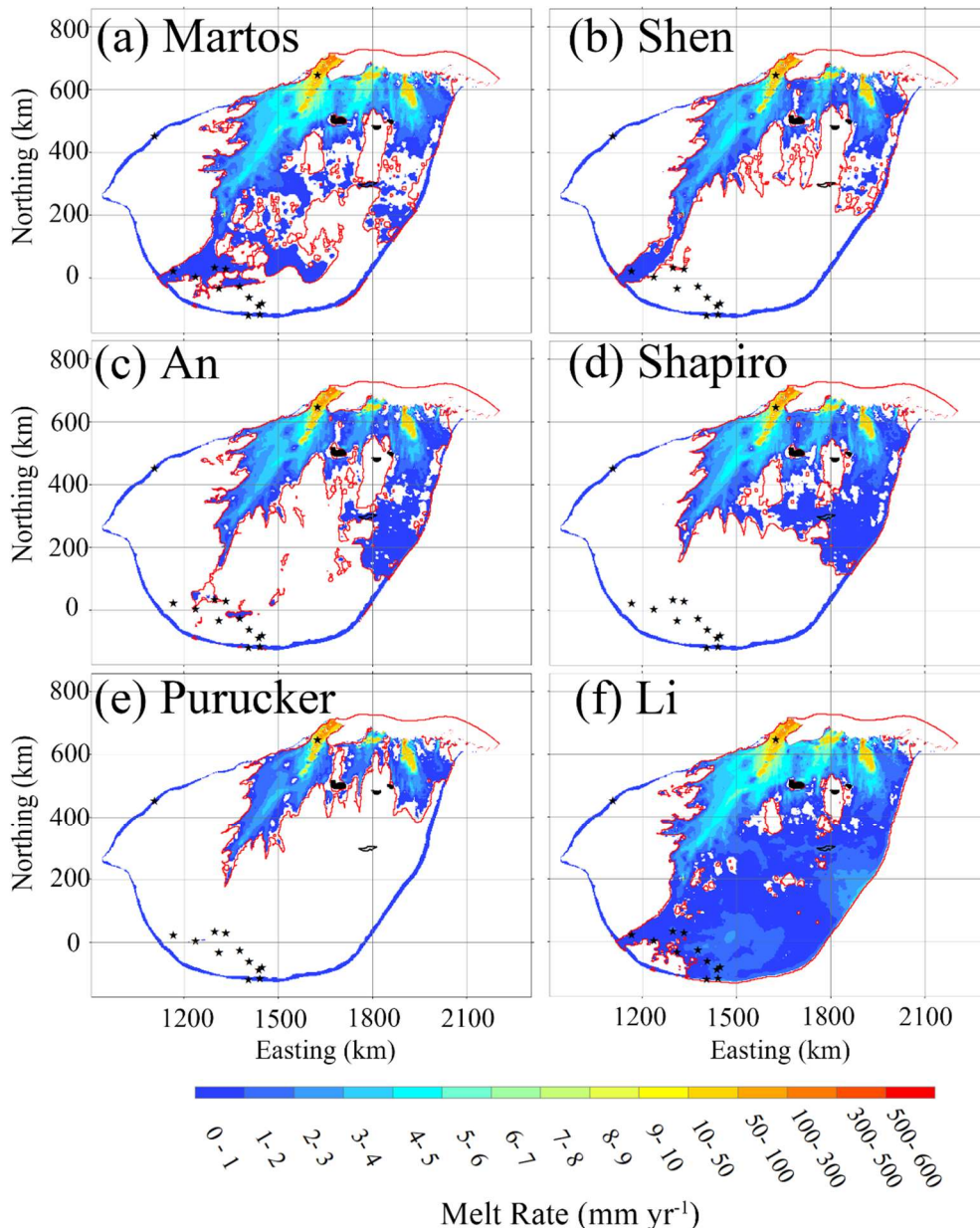
Fig. 9. Modelled basal melt rate (unit: mm yr^{-1}), (a) to (f) correspond to the GHF (a) to (f) in Fig. 2. The ice bottom at pressure-melting point is surrounded by a red contour. The stars denote the locations of observed subglacial lakes, and the area surrounded by the black line is the likely second largest subglacial lake in Antarctica. There is modelled basal refreezing at three local places painted in black.

485

5 Discussion

486 **5 Discussion**

487 Uncertainties and bias in our simulations can come from several sources. We expect
488 that the present-day accumulation rate field in our modelling will be higher than the
489 long-term average, because of lower accumulation rate during glacial periods
490 (Watanabe et al., 2003; Van Ommen et al., 2004). This will tend to increase the
491 downward advection of cold ice in our model, lowering the basal temperature in
492 comparison to reality. On the other hand, we also expect that the modern-day surface
493 temperature in our modelling will be higher than the long-term average temperature,
494 again because of lower temperatures during glacial periods. This will tend to increase
495 our modeled basal temperature in comparison with reality. It is unclear which of these
496 competing biases is stronger.

497

498 Subglacial topography has an influence on geothermal heat at kilometer scales.
499 Typically, it has been assumed that subglacial ridges receive less heat flow and
500 subglacial valleys receive more heat flow, in comparison to the regional average (e.g.,
501 van der Veen et al., 2007; Colgan et al., 2021). However, the effect depends on
502 subglacial rock type. Heat tends to follow the path of least resistance to the surface. The
503 thermal conductivity of rock varies with lithology, and can be either greater or smaller
504 than the thermal conductivity of ice (Willcocks & Hasterok, 2019), thus the sign of the
505 topographic effect on GHF can be either negative or positive. Without knowing a priori
506 whether the topographic effect will be positive or negative, it is hard to apply a
507 topographic correction field to the GHF input field.

508

509 GHF distribution largely governs basal thermal conditions. Many previous studies
510 (Larour et al., 2012; Pattyn, 2010; Pittard et al.,2016; Van Liefferinge and Pattyn, 2013;
511 Van Liefferinge et al. 2018) on basal temperature and basal melt have used the Shapiro
512 and Ritzwoller (2004), Fox Maule et al. (2005), Purucker (2013), and An et al. (2015)
513 GHF datasets, with few making use of the more recent Martos et al. (2017) and Li et al.
514 (2021) GHF datasets. In this study, we find that the Li et al. (2021) and Martos et al.
515 (2017) GHF datasets have higher GHF than the earlier datasets in the Lambert-Amery
516 domain and consequently have the largest area with warm base. The warmer basal
517 conditions best match the observed distribution of subglacial lakes. However, it should
518 be noted that observations of subglacial lakes are a one-sided constraint. A model result
519 that does not predict basal melt at the location of the observed lakes is clearly too cold
520 at that location. But if the model result shows basal melt at a place with no observed
521 lakes, it is not clear whether this is because the model is too warm, or the subglacial
522 water exists in a form other than ponded lakes, or that lakes are present, but we do not
523 have the data to detect them.

524

525 A lake complex beneath Devon Island ice cap in Canada exists at temperatures well
526 below pressure melting point due to large concentrations of dissolved salts (Rutishauser
527 et al., 2018), and no similar ones are known to exist beneath the Antarctic ice sheet.
528 Furthermore, relatively high electrical conductivity beds such as clay-rich sediments

529   surrounded by bedrock can give rise to false positives in radar detections of subglacial
530   water bodies (Tulaczyk et al., 2020).

531

532   Our simulations make improvements on previous approaches. We use the full-Stokes
533   flow model in the inversion of basal friction field rather than a simplified physics model
534   as in Wolovick et al. (2021a). We also improve on the treatment of the basal friction
535   field by imposing a larger basal friction where the ice bottom is colder than the pressure
536   melting point, and which increases with temperature difference from freezing point.
537   These modifications produce more physically meaningful results since we expect
538   frozen beds to have high basal friction. Hence, the basal friction field is constrained by
539   simulated temperatures in addition to producing the best fitting match of simulated and
540   observed surface velocities.

541

542   Van Liefferinge and Pattyn (2013) estimated basal temperature for the Antarctic ice
543   sheet using three GHF datasets (Fox Maule et al., 2005; Shapiro and Ritzwoller, 2004;
544   Purucker, 2013), and each of the datasets were improved by the method in Pattyn (2010).
545   Their modeled temperatures show spatial similarities to our experiment field using
546   Purucker et al. (2013) GHF. Pittard et al. (2016) did sensitivity experiments of the
547   Lambert-Amery glacial system based on 3 GHF fields (Fox Maule et al., 2005; An et
548   al., 2015; Shapiro and Ritzwoller, 2004) using the ice dynamics model PISM, and found
549   that modelled basal temperature reached the pressure melting point only under the fast-
550   flowing ice, with maximum melting rates of 500 mm yr^{-1} at places very close to the
551   grounding line of the central flowline onto the Amery ice shelf. We also model
552   maximum basal melt at similar locations in the six GHF experiments. However, the
553   Pittard et al. (2016) region of basal melt is mainly confined to the Lambert glacier
554   tributary and matches only that of our experiment using Purucker (2013) GHF.

555

556   We analyze the contribution of GHF and frictional heat to basal melt. The basal friction
557   is a significant heat sources only under fast-flowing ice. Most GHF distributions (except
558   Martos et al., 2017 and Li et al., 2021) in the grounded ice sheet near the ice shelf are
559   homogeneous, but frictional heating in the fast-flowing ice is more than 10 times higher
560   than that in the slow-flowing ice. Thus slower flowing ice in the interior of the ice sheet
561   is more sensitive to the GHF than fast-flowing ice (Larour et al., 2012).

562

563   GHF has its largest impact on the basal melt of the inland ice sheet. There are two
564   principle ways to constrain GHF: (1) direct measurement (2) inversion by multiple
565   geophysical methods. The GHFs used in this study are based on inversion of satellite
566   or aero magnetic data and seismic tomography. Direct observations of heat flux are
567   difficult to obtain in Antarctica, and satellite data are low resolution. The most efficient
568   method is to invert the heat flux through aerial geomagnetic observation such as for the
569   Martos and Li GHF fields (Martos et al., 2017; Li et al., 2021). However, there are still
570   large data gaps in remote regions, especially in PEL, leaving just inversion using
571   satellite magnetic data with a lower resolution. The Li et al. (2021) field uses the latest
572   aeromagnetic data to estimate the GHF in the PEL region and this gives higher values

573 than derived previously.
574
575 To validate the modelled basal melt, we use the locations of detected subglacial lakes.
576 There may be many other undiscovered subglacial lakes beneath the study area, and
577 further discoveries would help us validate the model results, and possibly refine GHF
578 maps. In addition, further observational constraints with a two-sided sensitivity to ice
579 temperature, such as observations of subglacial freeze-on or measurements of englacial
580 attenuation, would help us to identify areas in which the GHF maps are too warm, in
581 addition to those areas in which they are too cold.
582
6 Conclusions
583
584 In this paper, we estimate the basal thermal conditions of the Lambert-Amery system
585 by coupling a forward model and an inverse model, based on six different GHF datasets.
586 We analyze the contribution of GHF, heat conduction, and basal friction to the modelled
587 basal melt rate. We verify the result using the locations of all known subglacial lakes,
588 and evaluate the reliability of six GHF datasets in our study domain.
589
590 Our approach is distinct from that used to find GHF fields employed by Wolovick et al.
591 (2021a), in particular the use of a full Stokes model allows the method to be extended
592 to fast-flowing ice streams and ice shelf domains where neither the shallow ice nor
593 shallow shelf-approximations are valid. We also improve the basal friction calculation
594 to include information on the basal ice temperature relative to its pressure melting point.
595 This procedure results in removal of unrealistic noise manifested as local spikes in
596 modelled basal friction heat.
597
598 We find significant differences in the spatial extent of temperate ice in the slow flowing
599 areas among the six experiments due to large variability in GHF. The experiments using
600 Li et al. (2021) and the Martos et al. (2017) GHF yield the largest area with basal
601 melting, and match the subglacial lake locations best. In contrast, the experiments using
602 Purucker (2013) GHF gives the least area with basal melting and the worst match with
603 subglacial lakes locations. We suggest GHF datasets from Li et al. (2021) and Martos
604 et al. (2017) as the most suitable choice for this study region. We cannot make our own
605 GHF map from our analysis since while we can pick the GHF in places where the Li
606 and Martos geothermal heat flow maps (Li et al., 2021; Martos et al., 2017) are
607 consistent and both agree with the observations, we do not know which (if either) are
608 correct where the Li and Martos GHF datasets disagree and there are no observations.
609 In order to make this determination we would need additional observational constraints
610 on the basal thermal state, such as measured basal temperatures from deep ice cores, or
611 observed refreeze-on, but neither are available in the region.
612
613 The fast-flowing region has fast basal velocities and high frictional heat, but there are
614 large differences in basal melting rates between the 6 GHF datasets. The fast-flowing
615 tributaries have frictional heating in the range of 50-2000 mW m^{-2}. In the vast inland
616 areas, our experiments generally yield high upward heat conduction in the range of 45-

60 mW m^{-2} which means that GHF dominates the heat content of the basal ice in the slow flow regions. The modelled basal melt rate reaches 50-500 mm yr^{-1} locally in three very fast flow tributaries (Lambert, Lepekhin and Kronshtadtskiy glaciers) feeding the Amery ice shelf, and is in the range of 0-5 mm yr^{-1} in the inland region.

Data availability

All data sets used are publicly available.

Author contributions.

LZ and JM conceived the study. LZ, MW and JM designed the methodology. HK and LZ carried out the inverse model and produced the estimates and most figures. MW carried out the forward model and produced one figure. LZ wrote the original draft, and all the authors revised the manuscript.

Competing interests.

The authors declare no conflict of interest.

Acknowledgments

This work was supported by the National Natural Science Foundation of China (No. 41941006), National Key Research and Development Program of China (2021YFB3900105), and State Key Laboratory of Earth Surface Processes and Resource Ecology (2022-ZD-05).

References

An, M., Wiens, D. A., Zhao, Y., Feng, M., Nyblade, A. A., Kanao, M., et al.: Temperature, lithosphere-asthenosphere boundary, and heat flux beneath the Antarctic Plate inferred from seismic velocities, J. Geophys. Res.: Solid Earth, 120, 359-383, https://doi.org/10.1002/2014jb011332, 2015.

Arthern, R. J., Winebrenner, D. P., & Vaughan, D. G. Antarctic snow accumulation mapped using polarization of 4.3-cm wavelength microwave emission. Journal of Geophysical Research: Atmospheres, 111(D6), 2006, D06107. https://doi.org/10.1029/2004JD005667

Budd, W. F., Warner, R. C., Jacka, T., Li, J., and Treverrow, A.: Ice flow relations for stress and strain-rate components from combined shear and compression laboratory experiments, J. Glaciol., 59, 374-392, https://doi.org/10.3189/2013JoG12J106, 2013.

Colgan, W., MacGregor, J. A., Mankoff, K. D., Haagenson, R., Rajaram, H., Martos, Y. M., et al. (2021). Topographic correction of geothermal heat flux in Greenland and Antarctica. Journal of Geophysical Research: Earth Surface, 126, e2020JF005598. https://doi. org/10.1029/2020JF005598

Cuffey, K. M., and Paterson, W. S. B.: The physics of glaciers, fourth edition, Elsevier, Burlington, 2010.

Cui, X., Jeofry, H., Greenbaum, J. S., Guo, J., Li, L., Lindzey, L. E., et al.: Bed topography of Princess Elizabeth Land in East Antarctica, Earth Syst. Sci. Data, 12, 2765-2774, https://doi.org/10.5194/essd-2020-126, 2020a.

Cui, X., Lang, S., Guo, J., and Sun, B.: Detecting and Searching for subglacial lakes through airborne radio-echo sounding in Princess Elizabeth Land (PEL), Antarctica, E3S Web of Conferences, 163, https://doi.org/10.1051/e3sconf/202016304002, 2020b.

Diez, A., Matsuoka, K., Ferraccioli, F., Jordan, T. A., Corr, H. F., Kohler, J., Olesen, A. V., and Forsberg, R.: Basal Setings Control Fast Ice Flow in the Recovery/Slessor/Bailey Region, East Antarctica, Geophys. Res. Lett., 45, 2706–2715, 2018.

Dziadek, R., Ferraccioli, F., and Gohl, K.: High geothermal heat flow beneath Thwaites Glacier in West Antarctica inferred from aeromagnetic data, Commun. Earth Environ., 2, https://doi.org/ARTN 16210.1038/s43247-021-00242-3, 2021.

Fox Maule, C., Purucker, M. E., Olsen, N., & Mosegaard, K. (2005). Heat flux anomalies in Antarctica revealed by satellite magnetic data. Science, 309(5733), 464 – 467. https://doi.org/10.1126/science.1106888

Fretwell, P., Pritchard, H. D., Vaughan, D. G., Bamber, J. L., Barrand, N. E., Bell, R., et al.: Bedmap2: improved ice bed, surface and thickness datasets for Antarctica, The Cryosphere, 7, 375–393, https://doi.org/10.5194/tc-7-375-2013, 2013

Fricker, H. A., Siegfried, M. R., Carter, S. P., and Scambos, T. A.: A decade of progress in observing and modelling Antarctic subglacial water systems, Philosophical Transactions of the Royal Society A: Mathematical, Physical and Engineering Sciences, 374, 20140294, https://doi.org/10.1098/rsta.2014.0294, 2016.

Gagliardini, O., Zwinger, T., Gillet-Chaulet, F., Durand, G., Favier, L., Fleurian, B. d., et al.: Capabilities and performance of Elmer/Ice, a new-generation ice sheet model, Geosci. Model Dev., 6, 1299-1318, https://doi.org/10.5194/gmd-6-1299-2013, 2013.

Geuzaine, C., and Remacle, J. F.: Gmsh: A 3-D finite element mesh generator with built-in pre- and post-processing facilities, Int. J. Numer. Meth. Eng., 79, 1309-1331, https://doi.org/10.1002/nme.2579, 2009.

Greve R, Blatter H, Dynamics of Ice Sheets and Glaciers, Springer, 2009.

Gillet-Chaulet, F., Gagliardini, O., Seddik, H., Nodet, M., Durand, G., Ritz, C., et al.: Greenland ice sheet contribution to sea-level rise from a new-generation ice-sheet model, The Cryosphere, 6, 1561-1576, https://doi.org/10.5194/tc-6-1561-2012, 2012.

Gudlaugsson, E., Humbert, A., Andreassen, K., Clason, C. C., Kleiner, T., and Beyer, S.: Eurasian ice-sheet dynamics and sensitivity to subglacial hydrology, J. Glaciol., 63, 556–564, 2017.

Hansen, P., and Johnston, P.: Computational inverse problems in electrocardiology, 2000.

Jamieson, S. S., Ross, N., Greenbaum, J. S., Young, D. A., Aitken, A. R., Roberts, J. L., Blankenship, D. D., Bo, S., and Siegert, M. J.: An extensive subglacial lake and canyon system in Princess Elizabeth Land, East Antarctica, Geology, 44, 87–90, 2016.

King, M. A., Coleman, R., Morgan, P. J., and Hurd, R. S.: Velocity change of the Amery Ice Shelf, East Antarctica, during the period 1968–1999, J. Geophys. Res.-Earth, 112. doi:10.1130/g37220.1, 2007.

Larour, E., Morlighem, M., Seroussi, H., Schiermeier, J., and Rignot, E.: Ice flow sensitivity to geothermal heat flux of Pine Island Glacier, Antarctica, J. Geophys.

Res.-Earth, 117, https://doi.org/10.1029/2012jf002371, 2012.

Le Brocq, A. M., Payne, A. J., and Vieli, A.: An improved Antarctic dataset for high resolution numerical ice sheet models (ALBMAP v1), Earth Syst. Sci. Data, 2, 247-260, https://doi.org/10.5194/essd-2-247-2010, 2010.

Le Brocq, A. M., Ross, N., Griggs, J. A., Bingham, R. G., Corr, H. F. J., Ferraccioli, F., Jenkins, A., Jordan, T. A., Payne, A. J.,Rippin, D. M., Siegert, M. J., Evidence from ice shelves for channelized meltwater flow beneath the Antarctic Ice Sheet: Nat. Geosci., 6, 945–948, 2013.

Li, L., Tang, X., Guo, J., Cui, X., Xiao, E., Latif, K., et al.: Inversion of Geothermal Heat Flux under the Ice Sheet of Princess Elizabeth Land, East Antarctica, Remote Sensing, 13. doi:10.3390/rs13142760, 2021.

Malczyk, G., Gourmelen, N., Goldberg, D., Wuite, J., & Nagler, T.: Repeat subglacial lake drainage and filling beneath Thwaites Glacier. Geophys. Res. Lett., 47, e2020GL089658. https://doi.org/10.1029/2020GL089658, 2020.

Martos, Y. M., Catalán, M., Jordan, T. A., Golynsky, A., Golynsky, D., Eagles, G., et al.: Heat flux distribution of Antarctica unveiled, Geophys. Res. Lett., 44, 11,417-411,426, https://doi.org/10.1002/2017gl075609, 2017.

Maule, C. F., Purucker, M. E., Olsen, N., and Mosegaard, K.: Heat flux anomalies in Antarctica revealed by satellite magnetic data, Science, 309, 464-467, https://doi.org/10.1126/science.1106888, 2005.

Morlighem, M., Rignot, E., Binder, T., Blankenship, D., Drews, R., Eagles, G., et al.: Deep glacial troughs and stabilizing ridges unveiled beneath the margins of the Antarctic ice sheet, Nat. Geosci., 13, 132-137, https://doi.org/10.1038/s41561-019-0510-8, 2020.

Morlighem, M., Rignot, E., Seroussi, H., Larour, E., Ben Dhia, H., and Aubry, D.: Spatial patterns of basal drag inferred using control methods from a full-Stokes and simpler models for Pine Island Glacier, West Antarctica, Geophys. Res. Lett., 37, https://doi.org/10.1029/2010gl043853, 2010.

Mouginot, J., Scheuchl, B., and Rignot, E.: MEaSUREs Antarctic Boundaries for IPY 2007-2009 from Satellite Radar, Version 2, National Snow and Ice Data Center, 10, https://doi.org/doi:10.5067/AXE4121732AD, 2017.

Näslund, J.-O., Jansson, P., Fastook, J. L., Johnson, J., and Andersson, L.: Detailed spatially distributed geothermal heat-flow data for modeling of basal temperatures and meltwater production beneath the Fennoscandian ice sheet, Ann. Glaciol., 40, 95-101, https://doi.org/10.3189/172756405781813582, 2005.

Pattyn, F.: Antarctic subglacial conditions inferred from a hybrid ice sheet/ice stream model, Earth Planet. Sc. Lett., 295, 451-461, https://doi.org/10.1016/j.epsl.2010.04.025, 2010.

Pittard, M., Roberts, J., Galton-Fenzi, B., and Watson, C.: Sensitivity of the Lambert-Amery glacial system to geothermal heat flux, Ann. Glaciol., 57, 56-68, https://doi.org/10.1017/aog.2016.26, 2016.

Rutishauser A., Blankenship, D. D., Sharp, M., Skidmore, M. L., Greenbaum, J. S., Grima, C., Schroeder, D. M., Dowdeswell, J. A., Young, D. A., Discovery of a hypersaline subglacial lake complex beneath Devon Ice Cap, Canadian Arctic, Sci.

Adv.2018; 4: eaar4353

Purucker, M. E.: Geothermal heat flux data set based on low resolution observations collected by the CHAMP satellite between 2000 and 2010, and produced from the MF-6 model following the technique described in Fox Maule et al. (2005), 2012. Retrieved from http://websrv.cs.umt.edu/isis/index.php/Antarctica_Basal_Heat_Flux

Rezvanbehbahani, S., Stearns, L. A., Van der Veen, C. J., Oswald, G. K. A., and Greve, R.: Constraining the geothermal heat flux in Greenland at regions of radar-detected basal water, J. Glaciol., 65, 1023-1034, https://doi.org/10.1017/jog.2019.79, 2019.

Rignot, E., Mouginot, J., and Scheuchl, B.: MEaSUREs InSAR-based Antarctica ice velocity map, version 2, Boulder, Colorado USA. NASA National Snow and Ice Data Center Distributed Active Archive Center, https://doi.org/doi.org/10.5067/D7GK8F5J8M8R, 2017.

Rignot, E., Mouginot, J., Scheuchl, B., Van Den Broeke, M., Van Wessem, M. J., and Morlighem, M.: Four decades of Antarctic Ice Sheet mass balance from 1979-2017, P. Natl. Acad. Sci. USA, 116, 1095-1103, https://doi.org/10.1073/pnas.1812883116, 2019.

Shapiro, N. M., and Ritzwoller, M. H.: Inferring surface heat flux distributions guided by a global seismic model: particular application to Antarctica, Earth Planet. Sc. Lett., 223, 213-224, https://doi.org/10.1016/j.epsl.2004.04.011, 2004.

Shen, W., Wiens, D. A., Lloyd, A. J., and Nyblade, A. A.: A geothermal heat flux map of Antarctica empirically constrained by seismic structure, Geophys. Res. Lett., 47, https://doi.org/10.1029/2020gl086955, 2020.

Stearns, L. A., Smith, B. E., and Hamilton, G. S.: Increased flow speed on a large East Antarctic outlet glacier caused by subglacial floods, Nat. Geosci., 1, 827, 2008.

Tulaczyk, S. M., andeFoley, N. T.: The role of electrical conductivity in radar wave reflection from glacier beds, Cryosphere, 14, 4495-4506, 2020.

van der Veen, C. J., Leftwich, T., von Frese, R., Csatho, B. M., & Li, J. Subglacial topography and geothermal heat flux: Potential interactions with drainage of the Greenland ice sheet. Geophysical Research Letters, 34(12), 2007.

Van de Berg, W. J., Van den Broeke, M. R., Reijmer, C. H., & Van Meijgaard, E. Characteristics of the Antarctic surface mass balance, 1958-2002, using a regional atmospheric climate model. Annals of Glaciology, 41(1), 97-104, 2005. https://doi.org/10.3189/172756405781813302

Van Liefferinge, B., and Pattyn, F.: Using ice-flow models to evaluate potential sites of million year-old ice in Antarctica, Clim. Past, 9, 2335-2345, https://doi.org/10.5194/cp-9-2335-2013, 2013.

Van Liefferinge, B., Pattyn, F., Cavitte M. G. P., et al.: Promising Oldest Ice sites in East Antarctica based on thermodynamical modelling. The Cryosphere, 12, 2773-87, https://doi.org/10.5194/tc-12-2773-2018, 2018.

Van Ommen, T. D., Morgan, V., Curran, M. A. J., Deglacial and Holocene changes in accumulation at Law Dome, East Antarctic, Annals of Glaciology, 39, 359-365, 2004.

Watanabe, O., Shoji, H., Satow, K., Motoyama, H., Fujii, Y., Narita, H., and Aoki, S.: Dating of the Dome Fuji Antarctica deep ice core, Mem. Natl. Inst. Polar Res. Spec. Iss., 57, 25–37, 2003.

793 Willcocks, S., & Hasterok, D. Thermal refraction: Impactions for subglacial heat flux.
794 ASEG Extended Abstracts, 2019(1), 1–4. Taylor & Francis.
795 https://doi.org/10.1080/22020586.2019.12072986
796 Wolovick, M. J., Moore, J. C., and Zhao, L. Joint inversion for surface accumulation rate
797 and geothermal heat flow from ice-penetrating radar observations at Dome A, East
798 Antarctica. Part I: model description, data constraints, and inversion results, J. Geophys.
799 Res.-Earth, 126, 2021. https://doi.org/10.1029/2020jf005937, 2021a.
800 Wolovick, M. J., Moore, J. C., and Zhao, L. Joint inversion for surface accumulation rate
801 and geothermal heat flow from ice-penetrating radar observations at Dome A, East
802 Antarctica. Part II: Ice sheet state and geophysical analysis. Journal of Geophysical
803 Research: Earth Surface, 126, e2020JF005936, 2021b. https://doi.
804 org/10.1029/2020JF005936
805 Wright, A., and Siegert, M.: A fourth inventory of Antarctic subglacial lakes, Antarct.
806 Sci., 24, 659-664, https://doi.org/10.1017/s095410201200048x, 2012.
807 Zhao, C., Gladstone, R. M., Warner, R. C., King, M. A., Zwinger, T., and Morlighem,
808 M.: Basal friction of Fleming Glacier, Antarctica – Part 1: Sensitivity of inversion to
809 temperature and bedrock uncertainty, The Cryosphere, 12, 2637-2652,
810 https://doi.org/10.5194/tc-12-2637-2018, 2018.